JOURNAL OF MATERIALS RESEARCH AND TECHNOLOGY 2021;12:1319–1338

Available online at www.sciencedirect.com

jmr&t Journal of Materials Research and Technology

journal homepage: www.elsevier.com/locate/jmrt

Original Article

Structural, morphological and biological evaluations of cerium incorporated hydroxyapatite sol–gel coatings on Ti–6Al–4V for orthopaedic applications

B. Priyadarshini [a], S. Ramya [b], E. Shinyjoy [b], L. Kavitha [b,**,1], D. Gopi [c,***,1], U. Vijayalakshmi [a,*,1]

[a] Department of Chemistry, School of Advanced Sciences, Vellore Institute of Technology, Vellore, Tamilnadu, 632 014, India

[b] Department of Physics, School of Basic and Applied Sciences, Central University of Tamilnadu, Thiruvarur, Tamilnadu, 610 101, India

[c] Department of Chemistry, Periyar University, Salem, Tamilnadu, 636 011, India

ARTICLE INFO

Article history:
Received 31 October 2020
Accepted 1 March 2021
Available online 16 March 2021

Keywords:
Ti–6Al–4V
Ce-HAP coatings
Antibacterial
Bioactivity
Cell adhesion
Anti-corrosion

ABSTRACT

Titanium alloys, especially Ti–6Al–4V, were reported as a promising biomaterial featuring excellent corrosion resistance and good biocompatibility, but it lacks anti-infection capacity and osseointegration. In this work, we aimed to improve the bio-functions and corrosion resistance of AT-Ti-6Al–4V by applying cerium incorporated hydroxyapatite using a spin coater. The triple layer of Ce-HAP coatings was systematically accumulated using different speeds such as 2000, 3000 and 4000 RPM, which were sintered for 2 h at 500 °C. XRD and SEM-EDS characterize the developed Ce-HAP coatings to confirm the phase formation and surface morphology. The Colony Forming Unit confirms that Ce-HAP coatings exhibited significant inhibition efficiency towards the pathogens. *In vitro* bioactivity study evaluated in SBF indicates excellent apatite layer formation on Ce-HAP coatings. The cell viability studies using MG-63 cells showed good cell proliferation and attachments on a coated implant. The electrochemical properties of coatings were analysed by EIS and the result displayed pronounced anti-corrosion property. This study suggests that the cerium incorporated HAP promotes bioactivity with rapid osteointegration and presented higher corrosion resistance that makes it essential for the desired biomedical applications.

© 2021 The Authors. Published by Elsevier B.V. This is an open access article under the CC BY-NC-ND license (http://creativecommons.org/licenses/by-nc-nd/4.0/).

* Corresponding author.
** Corresponding author.
*** Corresponding author.
E-mail addresses: lkavitha@cutn.ac.in (L. Kavitha), dhanaraj_gopi@yahoo.com (D. Gopi), vijayalakshmi.u@vit.ac.in, lakesminat@yahoo.com (U. Vijayalakshmi).

[1] All the three corresponding authors have given equal contribution.

https://doi.org/10.1016/j.jmrt.2021.03.009

2238-7854/© 2021 The Authors. Published by Elsevier B.V. This is an open access article under the CC BY-NC-ND license (http://creativecommons.org/licenses/by-nc-nd/4.0/).

1. Introduction

In the last decades, biomaterials are used for re-establishing the functions of damaged or diseased human parts. Metallic materials, in particular, stainless steel, cobalt-chromium alloys, titanium and its alloys were widely used as medical implants, especially in orthopaedic surgeries like load-bearing application, hard tissue replacement, and fracture healing aid fixation devices [1,2]. Among these metals, titanium and its alloys (Ti–6Al–4V) proven to have excellent corrosion resistance, high biocompatibility with a prominent mechanical property, low toxicity, chemical stability and low young's modulus that made them be extensively used in orthopaedic surgery [3,4]. When exposed to air, this titanium alloy forms a highly stable oxide layer on its surface that has bone-bonding features with the implants. The excellent corrosion resistance of titanium appears due to passive film generation on the surface of alloys. For durable stability, bone im plants' surface properties are the primary factor for implant-bone tissue integration. However, Ti and its alloys exhibit smooth surfaces that have low bioactivity, reduced bone-bonding ability and wear resistance. In *vivo* conditions, these alloys leach Al and V ions into the body fluids that may be harmful to the living system [5,6]. To overcome these problems and expand the osteoconductivity, surface modification, namely bioactivation, anodization and hydroxyapatite coatings, can be employed on metal implant surfaces to ensure the natural bone at the implant-bone tissue interfaces [7].

Hydroxyapatite (HAP: $Ca_{10}(PO_4)_6(OH)_2$) is the main inorganic component of hard bone tissues, and it has wide application in biomedical engineering because of its excellent biocompatibility bond bonding ability and integrates with surrounding bone tissues [8,9]. It attracted attention as a surface coating due to their non-toxicity and osteoinduction. HAP promotes bone ingrowth as a component of filling materials for amputated bone and serves as a protective barrier to prevent leaching out of ions into the surrounding tissues [10–12]. HAP coated on titanium alloys are the most commonly used implants in orthopaedic and dental applications. The post-surgical removal of implants is the main problem associated with pure HAP coatings due to the bacterial accumulation on the implant surface, which leads to biofilm formation [13].

Consequently, to improve the properties of coatings viz bioactivity, mechanical property and anti-bacterial activity, HAP can be incorporated with various metal ions. Moreover, HAP structure allows ionic inclusion to imitate bone mineral functions and HAP-based bioactive materials improve the biological functions of coated implants. The bioactive metal ions such as Li^+, K^+, Ag^+, $Ce^{3+/4+}$, Cu^{2+}, CO^{2+}, Au^{3+}, Si^{4+}, and Cl^- based HAP coating on implants play a significant role in osteointegration [14,15].

Owing to its physicochemical property, cerium incorporated materials found attractive applications in various fields such as catalysis, corrosion prevention, electrochemical cells, photocatalysis, UV absorbers and optical, thermal behaviour [16]. Also, this element used in biomedical applications due to its excellent biological properties. It acts as a promising material in the treatment of burns. In *vitro* conditions, cerium proved to have excellent antibacterial and antimicrobial activity by interacting with the microbes' cell membrane. Besides, Ce has been used as an alternative material for corrosion inhibitors through cerium salts, leading to hydroxide formation, which sequentially reduces the rate of corrosion on implant materials [17].

The HAP-Cerium based deposition on titanium implants found to increase osteoblast integration with excellent biocompatibility [18–20]. Mathi et al. have fabricated cerium substituted HAP/PVP on Ti–6Al–4V alloys and the studies proved that the coatings improved corrosion resistance in SBF solution [21]. Gopi et al. developed dual substituted HAP with a combination of Ce^{3+}/Eu^{3+} on surgical grade stainless steel for better antibacterial activity and enhanced bioactivity [22]. Gabriela Ciobanu et al. developed cerium doped HAP/collagen coatings on commercially pure titanium to improve the osteointegration property for bone implants [23]. Qiuhua Yuan et al. fabricated cerium doped hydroxyapatite/PLA composite coating on stainless steel using a spin coating technique [24].

There are various approaches for developing metal ion-doped HAP coatings on implants, including plasma spray, ion beam, laser sputtering, spin coating and pulse laser deposition [25]. Among these coating techniques, the spin coating method is one of the most highly recommended methods for developing a thin film on metal substrates subsequently it has excellent adhesion strength between metal substrates and coatings, require of low sintering temperature, easier handling and low cost, it is a well-organized method of producing homogenous coatings with uniform thickness [26]. Developing HAP coatings using the sol–gel method depends on processing parameters like calcination temperature, layers of HAP, the chemical composition of the material, and substrates. Adhesion strength plays a crucial role in the substrate to coating interface for load-bearing applications. [27]. It depends on the roughness of the implants where the coatings can be deposited on the porous apertures of the implants substrate [28]. The surface roughness of implants can be increased by various surface treatments like sandblasting, acid etching, electrochemical polishing, etc. [29,30]. Therefore, in the present work, sol–gel-based, 1.25% Ce-HAP coatings were fabricated on Ti–6Al–4V by spin coating techniques. Their biological and electrochemical properties were examined to make the materials prominent in biomedical applications.

2. Experiments

2.1. Materials

Analytical grade Ti–6Al–4V alloy, Ceric (IV) ammonium nitrate [$(NH_4)_2$ Ce $(NO_3)_6$-SDFCL 98.5%], Calcium nitrate tetrahydrate [$Ca(NO_3)_2.4H_2O$-SDFCL 99%], Triethyl phosphite [$P(OC_2H_5)_3$-Sigma Aldrich 98%], Double distilled water [DD. H_2O], Phosphate buffer solution (PBS) and Dimethyl sulfoxide (DMSO).

2.2. Ti–6Al–4V surface treatment

The sheets of Ti–6Al–4V alloy in 10 × 10 × 3 mm coupons were used as a substrate material for Ce-HAP coatings. The chemical composition (wt%) of the Ti–6Al–4V alloy was: Al 6.7; V 4.21; O 0.14; Fe 0.10; Si 0.07; N 0.015; H 0.003; C 0.003 and residual Ti. For homogenous reaction, the Ti–6Al–4V samples were polished mechanically with 120–1200 grades of abrasive silicon carbide paper. The polished implants were cleaned with deionised water, followed by ultrasonic treatment in acetone for 20 min. The roughness of the metal implant surface was increased by acid treatment with a mixture of H_2SO_4: HCl: H_2O in 1:1:1 ratio at 60 °C for 1 h. Additionally, the Ti–6Al–4V samples were alkaline treated with 10 M NaOH at 60 °C for 24 h and oven-dried overnight at 45 °C.

2.3. Synthesis of sol–gel derived 1.25%Ce-HAP

Ammonium ceric nitrate $(NH_4)_2$ Ce $(NO_3)_6$, calcium nitrate tetrahydrate (Ca $(NO_3)_2.4H_2O$) and 0·6 M of triethyl phosphite (P $(OCH_2CH_3)_3$) were used as precursor materials, and they were dissolved in absolute ethanol. The molar ratio of calcium and cerium was maintained as 1.67. First, 0.6 M "P" precursors were stirred and refluxed for 8 h at 70 °C to initiate hydrolysis. 0.9875 M calcium (Ca^{2+}) and 0.0125 M ceric (Ce^{4+}) were stirred separately for 10 min, and the Ce + Ca mixture was added dropwise to the phosphate source and kept ageing for 24 h for calcium phosphate hydrolysis. Followed by refluxing at 85 °C for 16 h, the acquired solution was held for evaporation in the water bath to obtain viscous gel formed due to the polycondensation leads to Ca–O–P bonds formation.

2.4. Spin coating of 1.25% Ce-HAP on Ti–6Al–4V

The prepared 1.25% Ce-HAP sol with a 95 cP viscosity at 25 °C was deposited on alkali-treated Ti–6Al–4V substrate using a Spin NXG-P1 instrument. The Ce-HAP sol was coated on the surface of Ti–6Al–4V using different rotation speeds such as 2000, 3000 and 4000 RPM for 20 s. The rotation speeds have spread the sol to the entire surface, making the thin resin film on the substrates. The above process was repeated three times at a regular interval of 1 h drying in an oven at 100 °C. Finally, the obtained triple layer coated substrates were subjected to sintering at 500 °C for 2 h. Fig. 1 represents the image of the coatings developed at various RPM.

2.5. Wettability assay

The coating wettability was measured via the sessile drop method using DD water (Model Phoenix 300, SEO, Korea). This method was carried through dropping 1 μl of DD water on the coated surface, and testing was made by measuring the contact angle of water for 10 s. Wettability assay was done in triplicate, and the contact angle was observed by camera-based contact angle meter.

2.6. Vickers microhardness test

The microhardness of the coatings was determined by a Mitutoyo HM 210 B equipped with AVPAK- 20 V 2.0 software. The indentation load of 0.1–1.0 Kgf was used on surfaces for 15 s as dwelling time. The hardness calculated by dividing the load by the surface area of the indentation, such that Vickers hardness is determined using the following formula:

$$H_v = 1.844\ P/d^2\ (Kgf/mm^2). \quad (1)$$

where d is the average diagonal length of the indentation depth and P is the indentation test load. Indentation is made on the coatings by a diamond indenter through the application of a load P; where P represents the load in kgf (1 kgf = 9.8 N). (Fig. 7. (d)). The size 'd' of the resultant indentation, measured through the calibrated optical microscope, and the hardness is evaluated as the mean stress applied underneath the indenter. Five average measurements were carried out for each sample, and the average value was considered to avoid an error.

2.7. Pull off strength

The adhesive strength of the coatings spun at different RPM was measured using a universal testing machine ASTM F1044-05 (Shimadzu). In this method, Ce-HAP coated on Ti–6Al–4V substrates mounted on to the epoxy glue, and the non-coated surface was fixed to the metal rod. The adhesive strength was measured with a crosshead speed of 5 mm/min at a temperature of 175 °C. At maximum load, the coatings peeled off from the substrate. For each coating, three average measurements were considered to avoid data scattering.

2.8. Characterization of coatings

The phase composition of the coatings was tested by X-ray diffractometry (Bruker D8 Advance) with Cu–K radiation (1.5406 Å) in the scanning range 2θ range of 20°–90° and scanning rate of 1°/min. The substrate surface asperity was detected by using surface profilometer in order to quantify the surface roughness. Brookfield DV2T Viscometer (USA) measured the solution viscosity. The surface topography and cross-section of the bioceramic coated implant were examined using a scanning electron microscope (SEM: Hitachi S4800), and the chemical composition of the coatings was identified by EDS (Energy-dispersive X-ray spectroscopy).

2.9. *In vitro bioactivity study*

The apatite layer formation of Spin coated, 1.25% Ce-HAP on Ti–6Al–4V obtained at 2000–4000 RPM were immersed in 25 ml of simulated body fluid (SBF) for 10 and 20 days. The SBF solution was prepared by dissolving analytical grade chemicals NaCl, $NaHCO_3$, KCl, $K_2HPO_4{\cdot}3H_2O$, $MgCl_2{\cdot}6H_2O$, $CaCl_2$, Na_2SO_4, and $(CH_2OH)_3\ CNH_2\ {\cdot}HCl$ in double distilled water with pH maintained at 7.4 and stored in the refrigerator (Kokubo et al.). The ionic concentration of SBF is the same as in human blood plasma. The daily nourishment of SBF solution accomplished this immersion study in order to maintain the ionic concentration and avoid precipitation. After the post-determined incubation periods, the implants were removed from SBF solution and air-dried for overnight in oven followed by observation of bone apatite formation on the coated metal substrate by SEM.

2.10. *In vitro corrosion studies*

The corrosion restriction behaviour of bare Ti–6Al–4V, Alkali treated and all spin-coated samples was measured by electrochemical impedance spectroscopy (EIS) and potentiodynamic polarization technique (Tafel). The corrosion restriction of the substrate was determined by the electrochemical cell comprising of three-electrode setups, that includes the specimen of $1 \times 1\ cm^2$ functioning as a working electrode, platinum wire acting as a counter electrode (CE), silver/silver chloride (Ag/AgCl/Satd (KCl)) as a reference electrode (RE) (Biologic SA model SP-150, France). This experiment was carried out using an electrolyte solution simulated body fluid (SBF) with pH 7.4, where the ionic concentration of the SBF is equal to human plasma. The working condition for electrochemical impedance spectroscopy was measured using frequency ranging from 100,000 Hz–0.01 Hz with an amplitude of 10 mV at scan speed 10 points per decade. The potentiodynamic polarization curves were obtained at electrode potential −0.300 V to +0.300 V at a scan rate of 1Mv/min^{-1}. All the experiments were performed in triplicate to acquire average data.

2.11. *Colony-forming unit*

The colony-forming unit is the quantitative method to evaluate the bacterial restriction behaviour of coated Ti–6Al–4V alloy. The most infection-causing bacteria like (*E.coli*: ATCC 25922, *P. aeruginosa*: ATCC 27853) and gram-positive (*S.auerus*: ATCC 25923, *B. subtilis*: ATCC 23857) has been used as the test microorganisms. The bacterial suspension was obtained by overnight culturing bacterial cells in a lysogenic medium at 37 °C. From the above suspension, 2% was transferred to the side tube conical flask supplemented with nutrient broth and kept on an orbital shaker to attain the bacterial growth value of OD 0.5 measured using UV–Visible spectrophotometer (600 nm). This culture was further centrifuged at 6000 RPM for 5 min, followed by removal of supernatant and 10 ml of PBS buffer was added to the cell pellet. The prepared cell culture was serially diluted to the final concentration of 1×10^8 CFU/ml. All the samples Bare-Ti-6Al–4V, Alkali-Treated Ti–6Al–4V and 1.25% Ce-HAP spun at 4000 RPM were immersed in 5 ml of the cell culture and incubated at 37 °C for 24 h. After 24 h of incubation, the implant was removed from the culture followed by washing with PBS to remove the microorganism from the implant surface. Along with this, a negative control was inclined without the inclusion of any samples to the bacterial cell culture. Both the negative control and implant treated in bacterial culture were poured in the Muller Hinton agar medium contained in the Petri plates and incubated for 24 h at 37 °C. Finally, the developed number of colonies was measured using a digital colony counting unit. The formula calculated CFU/ml:

$$\mathrm{CFU} \Big/ \mathrm{ml} = \frac{C \times DF}{V} \tag{2}$$

where c is the number of colonies counted, DF is dilution factor and v is the volume of culture. The cell morphology of bacteria was observed under a Scanning electron microscope. The bacterial cells were seeded on the coated implants for 6, 12 and 24 h to perceive the cell adhesion. Posterior to the incubation, the implant was rinsed with PBS buffer, followed by a cell fixation using 2% of paraformaldehyde and 2% glutaraldehyde that was further dried under vacuum. Finally, the specimen was sputter-coated with gold/palladium and attended by Scanning Electron Microscope (SEM: Hitachi S4800).

2.12. *Cell line and culture*

MG-63 cell line was purchased from NCCS, Pune. The cells were preserved in Minimal Essential Medium enriched with 10% FBS, penicillin (100 μg/ml), and streptomycin (100 μg/ml) at 37 °C in a humidified atmosphere of CO_2.

2.12.1. *In vitro assay for proliferation activity (MTT assay) (mosmann, 1983)*

The MG-63 Cells (1×10^5/well) were fixed in 24-well plates and incubated at 37 °C with 5% CO_2 condition. Once after reaching the confluences, the samples were placed into the well plate containing cells and incubated for 24 h. After incubation, the sample was removed from the well and washed with Phosphate-Buffered Saline (pH 7.4). 100μl/well (5 mg/ml) of 0.5% 3-(4, 5-dimethyl-2-thiazolyl)-2, 5-diphenyl–tetrazolium bromide (MTT) was added to the samples and incubated for 4 h. Further, 1 ml of DMSO was added to the wells to remove the unreacted cells. The absorbance was measured at 570 nm with a UV- Spectrophotometer was DMSO serving as the blank. The Percentage (%) of cell viability was calculated using the formula:

$$\%\ \text{Cell viability} = \frac{\text{Experimental OD}_{570}}{\text{Control OD}_{570}} \times 100 \tag{3}$$

2.12.2. *Cell morphology*

The human osteoblast-like cells were culture on the coated metal substrates for incubation periods of 24, 48 and 72 h. After the completion of the incubation period, the MG-63 cells grown on the Ti–6Al–4V implant were rinsed off with 0.1 M PBS buffer and firmed with 2% of paraformaldehyde and 2% glutaraldehyde. Followed by the addition of 0.1 M sodium cacodylate buffer (pH 7.3) and incubated at 4 °C overnight. The

overnight cultured implant was removed and washed with ethanol several times to remove the non-adhered cells. Further, the coated implant was freeze-dried, followed by sputter coating with gold/palladium, and SEM observed the cell morphology.

2.13.1. *Dual AO/EB fluorescent staining*

Concisely, 5×10^5 MG-63 were seeded each 6-well plate allowed to adhere overnight. The cells were treated with Ce-HAP coatings on Ti–6Al–4V and incubated for 24, 48 and 72 h at 37 °C in a CO_2 incubator. The dual AO/EB fluorescent staining solution (1 μl) containing 100 μg/ml AO and 100 μg/ml EB (AO/EB, Sigma) was added to each suspension, and the morphology of apoptotic cells was examined via fluorescent microscope.

2.13.2. *Propidium Iodide staining*

MG-63 cells were seeded (one lakh cells per ml) in a 12-well plate and incubated for 24 h. After incubation, the monolayer of cells was treated with the coated metal sample (4000 RPM) and incubated for 24 h and 48 h. The treated metal substrates were washed with sterile PBS followed by cell fixing by 70% ethanol. 0.2 ml of Propidium Iodide (10 μg/ml) was added to the cells fixed on the coated metal substrates and left for 15 min. The stained substrates were removed from the 12-well plate and examined under a fluorescence microscope.

2.14. *Statistical analysis*

All the trials were performed in three folds to determine the concordant values, and the values were expressed in mean ± standard deviation (SD). Further, Graphpad 6.0 (two-way ANOVA) used for the statistical data analysis and $P < 0.05$ considered statistically substantial.

3. Result and discussion

3.1. *XRD analysis*

X-ray diffraction patterns of Ce-HAP coated on Ti–6Al–4V at 2000–4000 RPM are shown in Fig. 2. The microstructure of Ti–6Al–4V contains two lamellae α and β phase that possess high mechanical strength, ductility, plasticity and weldability. The diffraction pattern for the Ti–6Al–4V given in Fig. 2 (a), the Miller indices and phase formation were derived from α-Ti and β-Ti according to the **JCPDS#44–1294, JCPDS#44–1288** [31,32]. Although Ti–6Al–4V inevitably undergoes passivation by creating a thin oxide layer reflected in the XRD analysis by the presence of only Ti peak. It was further noted that weak β phase reflection, indicating a low volume fraction of the β phase. The XRD diffraction pattern corresponding to the 1.25% Ce-HAP spun at 2000, 3000, 4000 RPM were depicted in Fig. 2 (b-d). From Fig. 2 (b-d), a superposition of two different diffractograms was detected, which corresponds to the HAP and Ti presence. Doping of Ce into the HAP lattice and its coating on the Ti substrate does not show any transformation, impurities and decomposition. All the diffraction peaks were exactly matched with the JCPDS#09–0432 (a = 9.418 Å and c = 6.884 Å). The distinguished peaks at 2θ regions of 25, 28, 31–33 and 40°–56°, concord with the hexagonal (space group P63/m) crystal structure of HAP. The presence of calcium phosphate in coating mimics the natural bone through the osteointegration process. The coating decomposition may occur at low sintering temperatures due to ion migration from the substrate [33,34]. In contrast, at the higher sintering temperature, it results in the development of secondary phases like β-TCP and other calcium carbonates. Hence, the prepared triple layer coating sintered at 500 °C does not show any disintegration. As the increase in the RPM, the triplet peak intensity of HAP increases with a decrease in the Ti. The increase in the crystallinity of HAP denotes coating prone to less dissolution under *in vitro/in vivo* condition. From Fig. 2 (d), the distinct behaviour that was observed concerning the HAP crystallinity was significantly higher than Ti (4000 RPM). Due to the coating's durable thickness, strong HAP peak intensity was detected that disguised Ti peak orientation at 39° and 40.5°. These results indicate the formation of Ce-HAP on the Ti–6Al–4V with its characteristic peaks that was further evidenced by the other analytical techniques.

3.2. *Surface roughness and surface morphology*

The surface roughness of Ti–6Al–4V, alkali-treated and coated metal substrates were given in Table 1. It is necessary to impact surface roughness on Ti–6Al–4V for excellent mechanical strength that anchor Ce-HAP on to the substrate. The surface roughness recorded for alkali-treated metal are $R_a = 5.58 \pm 0.54$; Ce-HAP coating displayed roughness of 4.78 ± 1.2 @2000; 3.32 ± 0.8 @3000; 2.54 ± 0.8@4000 RPM. Surface roughness is an essential criterion for determining bone-to-implant contact, cell attachment, proliferation, tissue response, and protein flow tuning *in vivo* condition.

The surface topography of the non-coated and coated Ti–6Al–4V was analysed using a scanning electron microscope and displayed in Fig. 3a. and Fig. 3b. From Fig. 3a. The surface morphology of as polished bare Ti–6Al–4V metal exhibited rough surface with few cracks due to grit polishing, whereas alkali-treated metal clearly showed a porous network. It was noted that treatment with NaOH dehydrates and induces a porous network structure on the implant surface. Huynh et al. reported that post-treatment with NaOH on the substrate improves the bone-bonding ability with the surrounding tissue due to increased surface area (34). According to **Lee** et al., **(2002),** the presence of a porous network leads to local corrosion as a virtue of production of OH^- radical on the Ti–6Al–4V surface. The acid treatment with HCl and H_2SO_4, followed by alkaline treatment (NaOH), increases the osteointegration property with a better healing process during the initial implantation. Grit blasted surface treated with an alkaline solution can create small uniform pits on the metal surface, evidenced in Fig. 3a.(b). Additionally, the absence of Na peaks detected for Alkali treated metal has been noted. This was due to the non-thermal treatment of metal after alkali treatment. Kobayashi et al and Liu et al. reported that Alkali treatment followed by thermal treatment at 500 °C forms sodium titanate hydrogel layer, which is stable without the transformation of titanium oxide [35,36]. Fig. 3b. Signifies

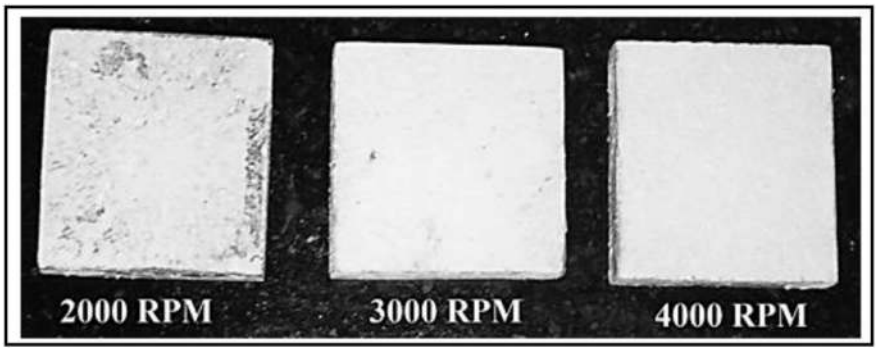

Fig. 1 – Photograph of coatings obtained at different RPM.

the triple layer coating produced at a different spin rate of 2000, 3000 and 4000 RPM, representing surface morphology depends on the deposition parameters. There were voids and crack spotted throughout the surface of the coating sintered at 500 °C developed at 2000 RPM. This may be due to dehydration on the coating surface, which may be the reason for the generation of cracks. **Hamalaoui** et al. projected the development of cracks on coating due to the air bubble formation during the dehydration process and shearing stresses on heat treatment [37]. In Fig. 3b. (b) layers of the grain boundaries were perceived for the coating produced at 3000 RPM, whereas for coating produced at 4000 RPM, a more uniformly smooth surface with crack free and without any gap interface was obtained as shown in Fig. 3b. (c). This indicates the strong chemical bonding between the sol–gel derived Ce-HAP coatings and Ti–6Al–4V substrates. The surface topography distinguishes variation in the coating surface based on the deposition parameters. EDS spectra confirm the presence of Ti, Al, and V absence of oxygen perceived on the bare Ti–6Al–4V. The presence of an oxide layer on titanium and its

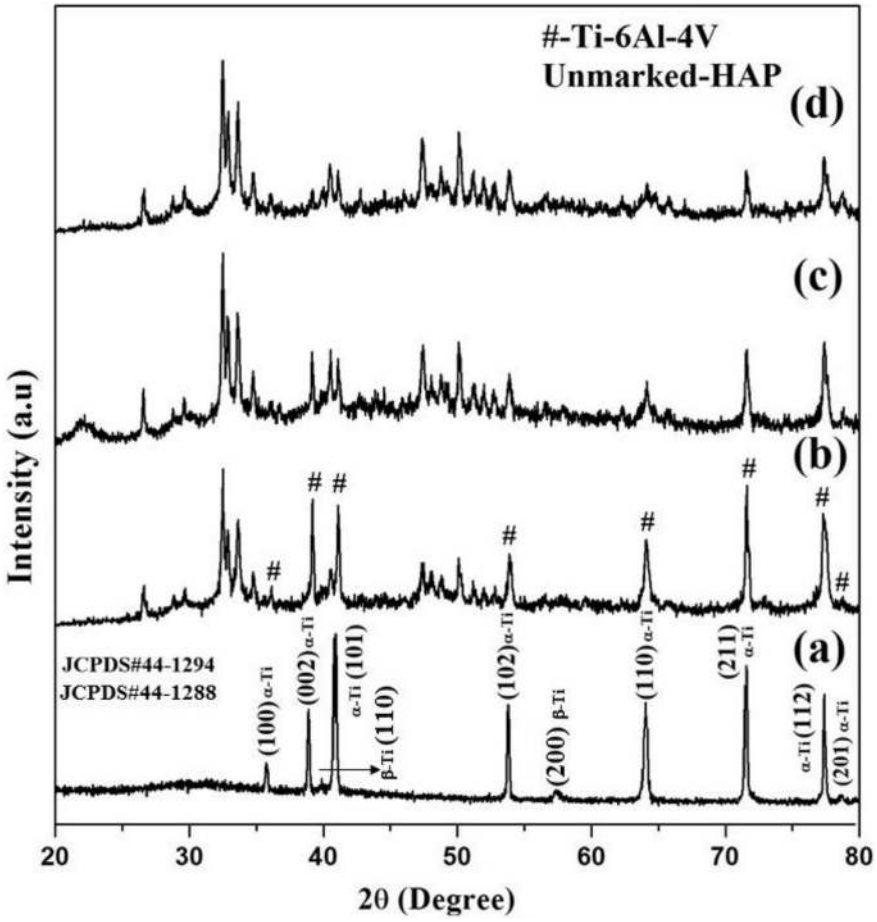

Fig. 2 – XRD analysis of, Ti–6Al–4V (a) 1.25% of Ce-HAP coated on Ti–6Al–4V obtained at 2000 RPM (b), 3000 RPM (c), 4000 RPM (d).

Table 1 – Surface roughness of uncoated and coated Ti–6Al–4V substrates.

Modification process	Ra (μm) surface roughness
Bare Ti–6Al–4V	1.56 ± 0.9
AT- Ti6Al–4V (Alkali treated)	5.58 ± 0.54
2000 RPM	4.78 ± 1.2
3000 RPM	3.32 ± 0.8
4000 RPM	2.54 ± 0.68

alloy was in nano range that cannot be detected through EDS spectra. Further, for the alkali-treated metal–oxygen peak along with Ti, Al, and V were perceived. The triple layer Ce-HAP coatings EDS confirm the presence of Ti, Al, V, O, Ca, P and Ce peaks. This shows the formation of homogeneity and uniform coating can be achieved at 4000 RPM using spin-coating techniques.

3.3. *Bioactivity of coatings*

In vitro bioactivity of the coatings was investigated by immersing the coated implant in SBF solution for 10 and 20 days. Further, the SBF immersed sample was observed under a scanning electron microscope, and it is shown in Fig. 4a. Fig 4a. (a-c) Shows 10 days SBF immersed sample, and the result revealed a cluster of apatite to form coarse granular

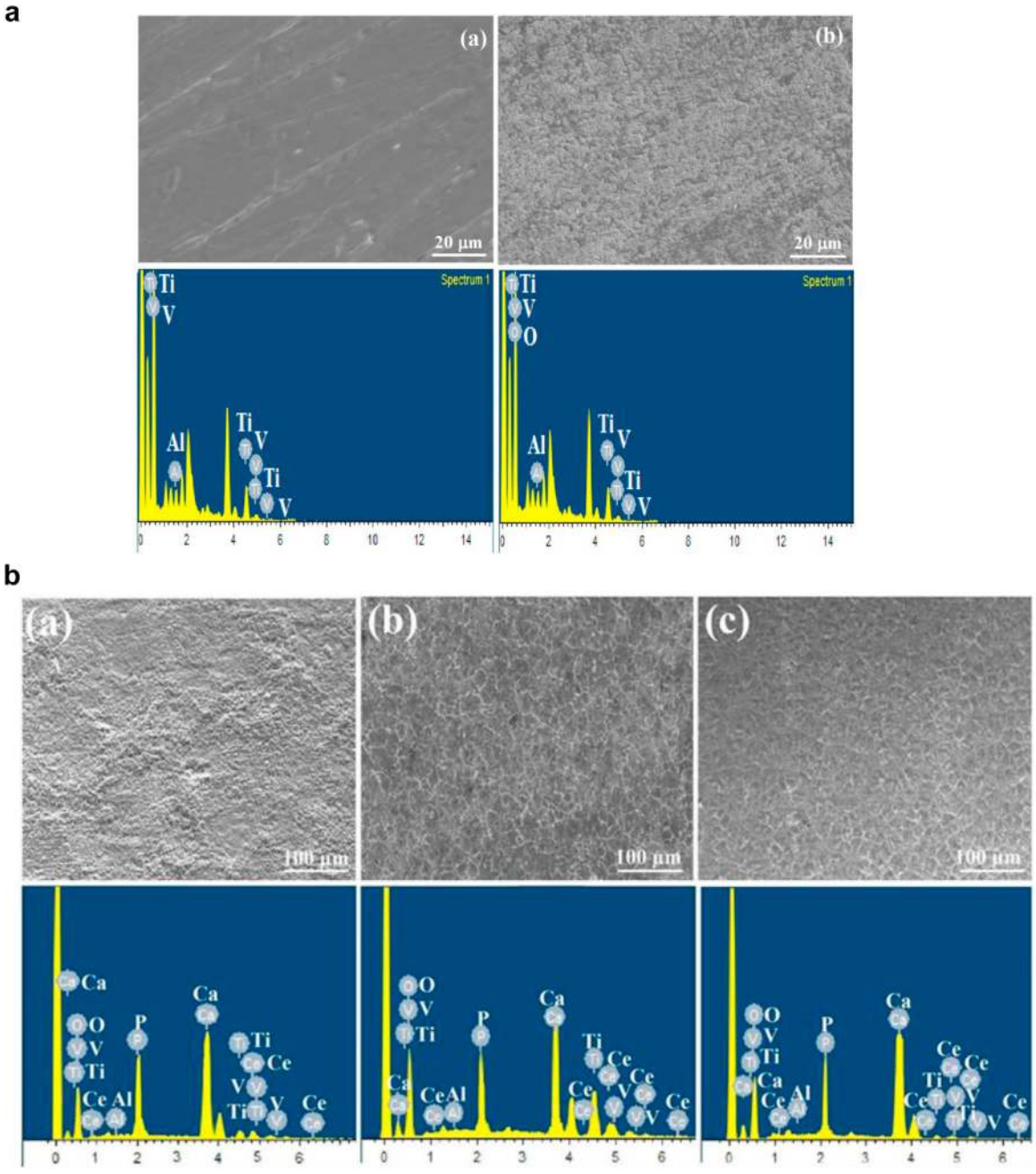

Fig. 3 – a SEM Micrographs and EDS analysis of bare Ti–6Al–4V and alkali treated Ti–6Al–4V. b. SEM Micrographs and EDS analysis of 1.25% of Ce-HAP spin coated at 2000 RPM (a), 3000 RPM (b), 4000 RPM (c).

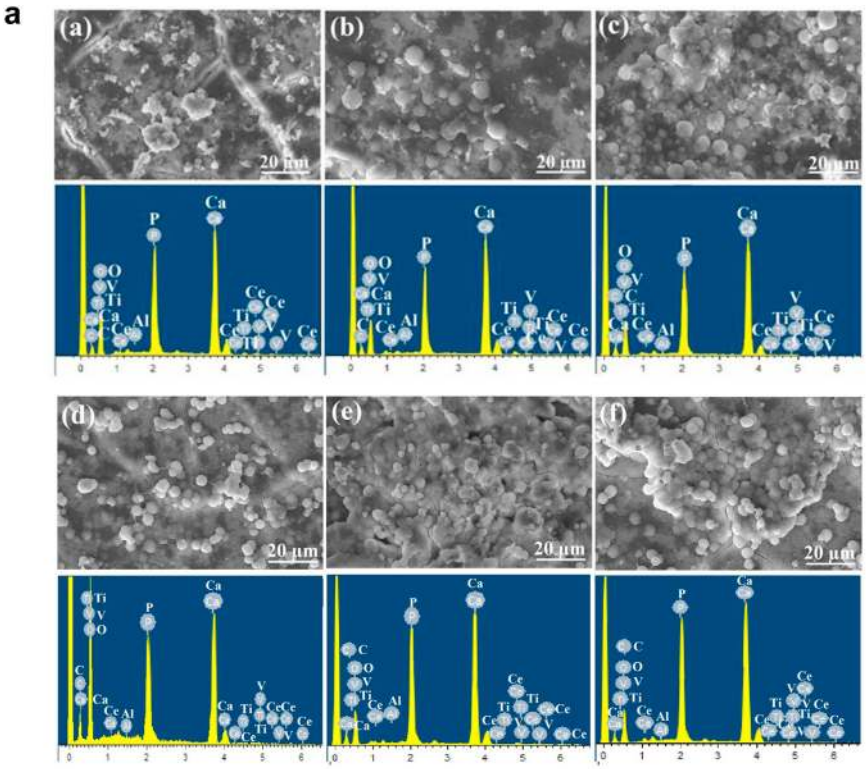
a
(a)
(b)
(c)
(d)
(e)
(f)
20 μm
Ca
P
O
V
Ti
Ce
Al
C

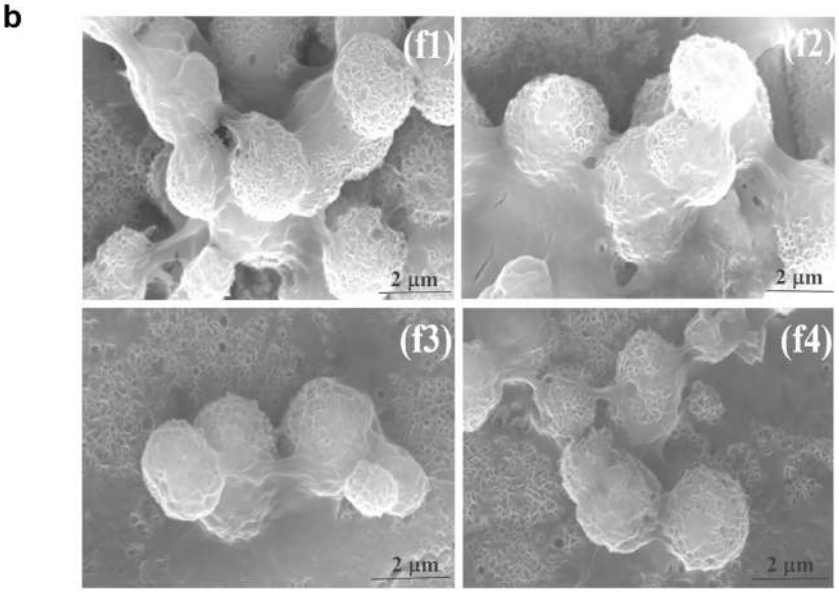
b
(f1)
(f2)
(f3)
(f4)
2 μm

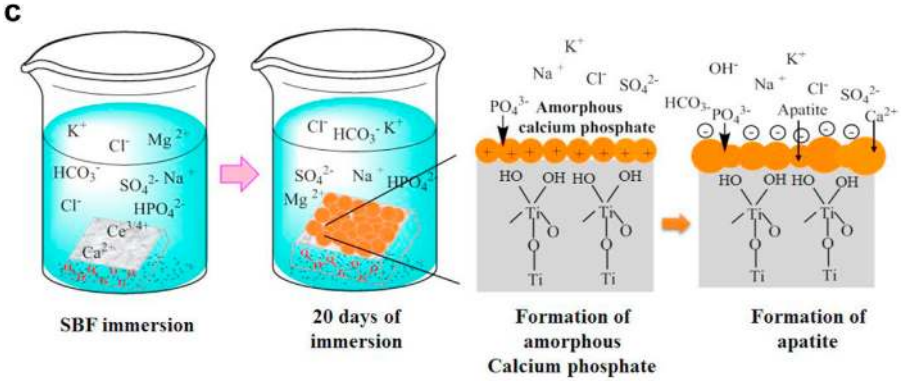
c
SBF immersion
20 days of immersion
Formation of amorphous Calcium phosphate
Formation of apatite
Amorphous calcium phosphate
Apatite
HO
OH
Ti
O

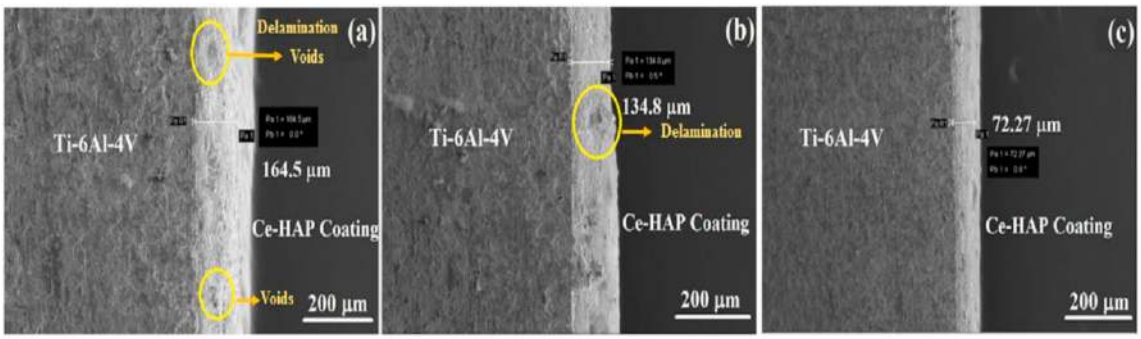

Fig. 5 – Cross-sectional view of Ce-HAP coated on Ti–6Al–4V obtained at 2000 RPM (a), 3000 RPM (b), 4000 RPM (c).

aggregates on the surface, which was similar for all the coating soaked in SBF. Furthermore, Fig. 4a. (d-e) It showed 20 days immersion with the formation of secondary spherical shaped apatite, which was homogeneously spread on the coated implant surface. The apatite clusters grew up fast in the rows on the surface, especially for 20 days of immersion. Additionally, at higher magnification coral-like structure was perceived for sample spun at 4000 RPM that was shown in Fig. 4b. This demonstrates that the Ce-HAP induce surface activity through the nucleation process, followed by apatite growth. The presence of dopant (Ce) makes hydroxyapatite more precipitate to aggregate by stabilizing HAP, thus inhibiting decomposition. The EDS spectra analyzed the elemental analysis of the SBF immersed sample. After 10 and 20 days of immersion periods, the entire sample showed the existence of Ti, Al, V, Ca, O, P and Ce on the coated metal surface. This EDS analysis suggests that cerium ions were incorporated in the hydroxyapatite structure, which was deposited on the titanium surface and apatite formations.

The mechanism of bone apatite formation on the substrate in the SBF was schematically illustrated in Fig. 4c. The doping of Ce into HAP lattice might cause alteration in properties like solubility and thermal stability, enhancing the biomineralization and dissolution for apatite formation. The actual metabolism of the apatite formation in the SBF was previously reported by **Heshmatpour F** [38]. Ionic activity plays a significant role in the development of the bone-like apatite on the surface by increasing the concentration of ions and pH of the solution. The Ca^{2+} and Ce^{4+} ions present in the coating undergoes ionic exchange with oppositely charged ions by the electrostatic interaction on the Ti–OH based surfaces. The hydroxyl groups present in calcium phosphate induce the apatite nucleation on the Ce-HAP surface. The negatively charged group, such as PO_4^{3-} and OH^- ions in SBF diffuse to both surfaces, results in an amorphous calcium phosphate layer. Finally, the apatite layer was found to cover the entire interface of the coatings throughout the immersion process. According to **Kokubo** et al. human body fluids are highly supersaturated, leading to the growth of nucleation concerning apatite formation. Surface area, density, and structure of

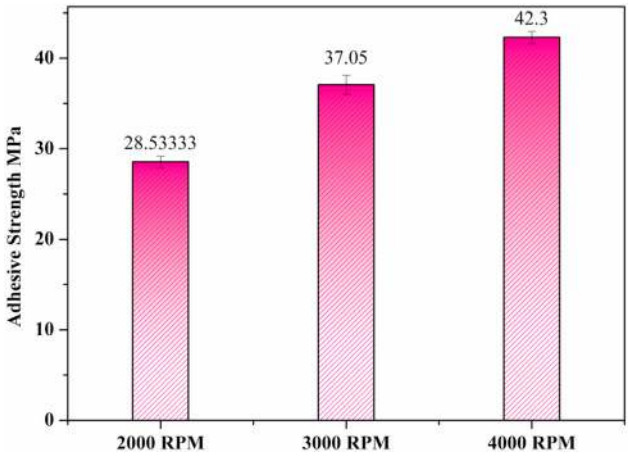

Fig. 6 – Adhesion strength of the coatings obtained at 2000 RPM, 3000 RPM and 4000 RPM.

coatings are responsible for the nucleation of apatite on the biocompatible surface [39]. The result of the Ce-HAP coating suggests the nucleation of the surface increases with respect to the immersion times. The ICP-OES analysis detected the ion release from the coating the data are predicted in the supplementary information.

3.4. *Cross-sectional study*

The coating thickness depends on the number of the layer spun on the surface of the alkali-treated Ti–6Al–4V. The triple layer coating thickness was measured by the cross-sectional view via the SEM micrograph and prophesied in Fig. 5. The average thickness of the coating from SEM images is 164.5, 134.8, and 72.27 μm for 2000, 3000 and 4000 RPM, respectively. Fig. 5 (a-b) shows Ce-HAP coatings on Ti–6Al–4V obtained at 2000 and 3000 RPM. It was observed that the coatings were non-uniform with delamination might have caused due to the decomposition of the organic matter present in Ce-HAP during thermal treatment. The complete overlap of coating with Ti–6Al–4V without delamination, voids, or crack between the

Fig. 4 – a. Surface morphology and EDS analysis of SBF immersed 1.25% of Ce-HAP coated on Ti–6Al–4V 2000 RPM (a), 3000 RPM (b), 4000 RPM (c) for 10 days and (d–e) for 20 days. b. Higher magnification SEM micrograph of apatite formation on the surface of Ce-HAP coatings on Ti–6Al–4V obtained at 4000 RPM (20 days). c. Schematic Representations of surface changes and apatite formation on the surface of Ce-HAP coated on Ti–6Al–4V in an SBF solution.

Table 2 – Electrochemical impedance values of Bare, alkali- and Ce - HAP-coated Ti–6Al–4V produced at different RPM in SBF solution.

Sample Descriptions	R_s (Ω cm^{-1})	R_{ct} (Ω cm^{-1})	C_{dl} (F/cm^2)	n	E_{corr} (mV)	I_{corr} (μA/cm^2)
Bare Ti–6Al–4V	12.63	6731	$85e^{-6}$	0.774	−112.061	2.116
Alkali treated Ti–6Al–4V	14.48	8871	$69.88\ e^{-6}$	0.768	−86	1.509
1.25% Ce-HAP 2000 RPM	37.08	26810	$52.616\ e^{-6}$	0.786	−135	0.485
3000 RPM	43.08	35105	$44.1\ e^{-6}$	0.830	−109	0.414
4000 RPM	143.7	257358	$38.77\ e^{-6}$	0.849	−97	0.047

Ce-HAP and Ti alloy interface were identified for the coatings developed at 4000 RPM. The parallel line between the alloy and the coating denotes substrate coating interaction formed by lamellar deposition. Also, it signifies the diffusion of coatings through the porous structure, thereby enhances adhesion strength. This suggests that a thin film of Ce-HAP with the uniform thickness could be accomplished by using spin coating and emphasize for bone grafting applications.

3.5. *Adhesion strength*

Adhesion strength depends on the composition of the coatings and surface roughness. It plays a significant role in some circumstances where coatings' delamination occurs between the interface of the Ti–6Al–4V metal substrates. Hence bond strength of Ce-HAP coatings was determined using Peel off test, and the result was given in Fig. 6. The bond strength was determined as follows 28.53 ± 1.10, 37.05 ± 1.48 and 42.5 ± 1.17 MPa corresponds to 2000, 3000 and 4000 RPM, respectively. Previously it was reported that the bond strength of alkali-treated metal and its coatings appeared to have greater adhesion strength due to the porosity created on the metal surface [40]. Moreover, it was observed that the coatings developed at 2000 RPM has weak adhesion strength due to the quality of the increased crack exposure and relatively reduced strain causes delamination compared with other films on Ti–6Al–4V. The diminished bond strength value between interfacial of coating and metal substrates related to the deformation and stress created on the substrates that deemed to impersonate in the delamination of coatings. The enhanced adhesion strength of coating produced at 4000 RPM showed increased bond strength due to the incorporation of Ce^{4+} ion into HAP lattice, which can reinforce grain boundaries by reductions in the energy and uniformity, compact behaviour. The combination of metal ions, the structure of the material and interfacial interactions enhance the adhesion strength. Zeng et al. reported that excellent bond strength could be achieved by sol–gel derived coating on the metal substrates than any other technique [41].

3.6. *Wettability*

Biological macromolecules like protein flow, cell adhesion, migration, platelet adhesion, blood coagulation and tissue growth of the biomedical implant depend on the wettability nature of the implants. For biological cell immobilization, wettability plays a major role, and contact angle hysteresis (Δθ) used to investigate the properties of the non-coated Ti–6Al–4V, Alkali treated Ti–6Al–4V and Ce-HAP coating, and the results were given in Fig. 7. (a). The surface of the non-coated Ti–6Al–4V showed a contact angle of 74.05° ± 2.12, which indicates hydrophobic nature. In contrast, alkali-treated Ti–6Al–4V showed a contact angle of 32.8° ± 2.42, reveals the hydrophilic nature due to NaOH treatment that could create a rough surface by inducing grooves throughout the substrate. Acid itching followed by alkaline treatment accompanied by surface chemical reactions alters the material property by creating the pores that contribute to the hydrophilic structure of Ti–6Al–4V. As a result, variation in the wettability of the sample was induced by these chemical techniques. The contact angle for the Ce-HAP coatings obtained at 2000, 3000 and 4000 RPM was measured as 11.04° ± 1.6, 15.05° ± 1.09, and 22.02° ± 2.08 indicating the nature of improved wettability. Reduced hydrophilic nature for the coating produced at 2000, and 3000 RPM was due to cracks and surface roughness. The hydrophilicity of Ce-HAP depends on the chemical composition of HAP that contains a higher amount of hydroxyl groups, which is hydrophilic. Hence all the coatings have shown hydrophilic nature compared to bare. The Ti–6Al–4V were hydrophobic with the contact angle of 74.05° ± 2.12, while for the coating derived at 4000 RPM, the contact angle had an affinity to decrease to 22.02° ± 2.08. Previous studies reported the hydrophilic surface induces cell growth and protein flow than the hydrophobic surface. Thus, the contact angle measurements indicated the hydrophilic properties of the sol–gel derived Ce-HAP coating. **Webb** et al. described that with moderate hydrophilicity of contact angle between 20 and 40° were found to have good cell growth and cell attachments [42]. Hence, the obtained Ce-HAP coatings developed at 4000 RPM have a contact angle of 22.02° ± 2.08 can be used for orthopaedic implantation due to its uniformity, and this may enhance the cell proliferation and spread of cells on Ce-HAP coating.

3.7. *Vickers microhardness*

For long-term orthopaedic applications, it is crucial to study the hardness of the materials to avoid the implant's failure. Vickers indentation hardness test was carried out on the flat-coated surface at different load indents of 0.1, 0.2, 0.3, 0.5, and 1.0 kgf, which depicted in Fig. 7 (b) and Table 3. From Table 3, the hardness value of the coating derived at 4000 RPM exhibited a value of 491.2 MPa at low load (0.1 kgf) and 260.53 MPa at a high load of 1.0 kgf. The 3000 RPM coated substrates have a hardness value of 442.06 (low load) to 231.4 MPa (high load), whereas the coating derived at 2000 RPM has shown the value of 367.6 (low load) to 166.4 MPa (High load). The hardness commonly referred to as indentation size

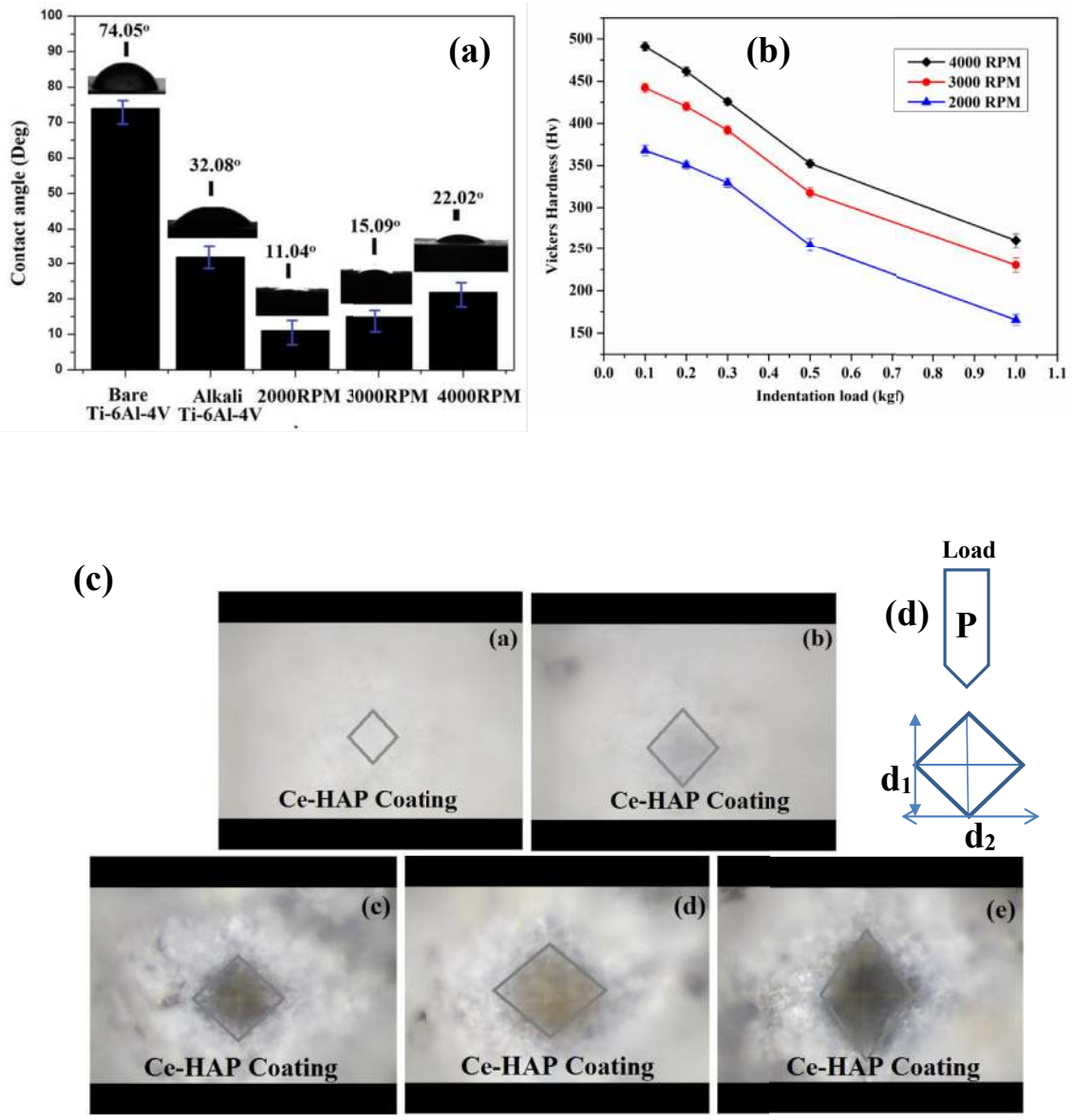

Fig. 7 – (a) Contact angle measurements (b) Vickers hardness measurements Ce-HAP coatings produced at different RPM. (c) Optical images of the micro intended surfaces of coated Ti–6Al–4V substrates produced at 4000 RPM at 100 g (a), 200 g (b), 300 g (c), 500 g (d) and 1000 g (e). (d) Vickers microhardness test scheme, P = Load in kgf d = Arithmetic mean of the two diagonals, d_1 and d_2 in mm.

defect (ISE) caused by indentation friction and elastic deformation that occurs after loading. The hardness value was found to decrease with the increase in the load and it depends on the surface area to volume ratio of indentation load. Reduced hardness for coating obtained at 2000 RPM at low-load was due to the propagation of cracks, voids and burst dislocation. Compared with all the other coatings, the maximum hardness was obtained for the coating at 4000 RPM at a high load of 1.0 kgf (356.53 H_v). It was examined that the loading value was different for the same material with different loads this behaviour was due to the hardening deformation of the materials. At smaller indentation size, the hardness value was found to be higher, and at larger

Table 3 – Vickers Microhardness for the coatings obtained at various parameter.

Sample code	0.1 Kgf	0.2 Kgf	0.3 Kgf	0.5 Kgf	1.0 Kgf
4000 RPM	491.2 ± 5.2	461.5 ± 5.2	425.63 ± 4.0	352.4 ± 4.6	260.53 ± 8.0
3000 RPM	442.06 ± 5.3	419.96 ± 5.2	391.96 ± 5.0	317.7 ± 6.0	231.4 ± 8.0
2000 RPM	367.6 ± 6.0	350.7 ± 4.3	329.53 ± 5.3	255.23 ± 8.3	166.4 ± 6.04

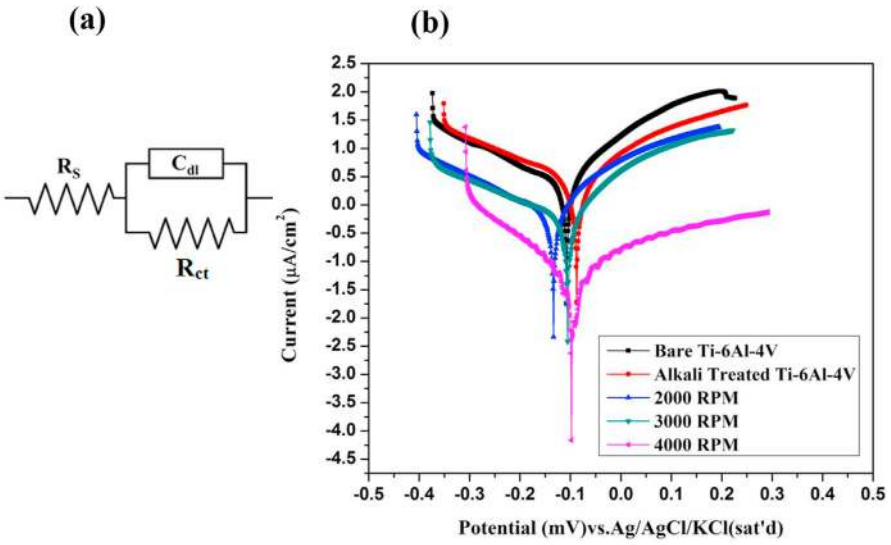
(a)
(b)
R_S
C_{dl}
R_{ct}
Current (μA/cm²)
Potential (mV)vs.Ag/AgCl/KCl(sat'd)
Bare Ti-6Al-4V
Alkali Treated Ti-6Al-4V
2000 RPM
3000 RPM
4000 RPM

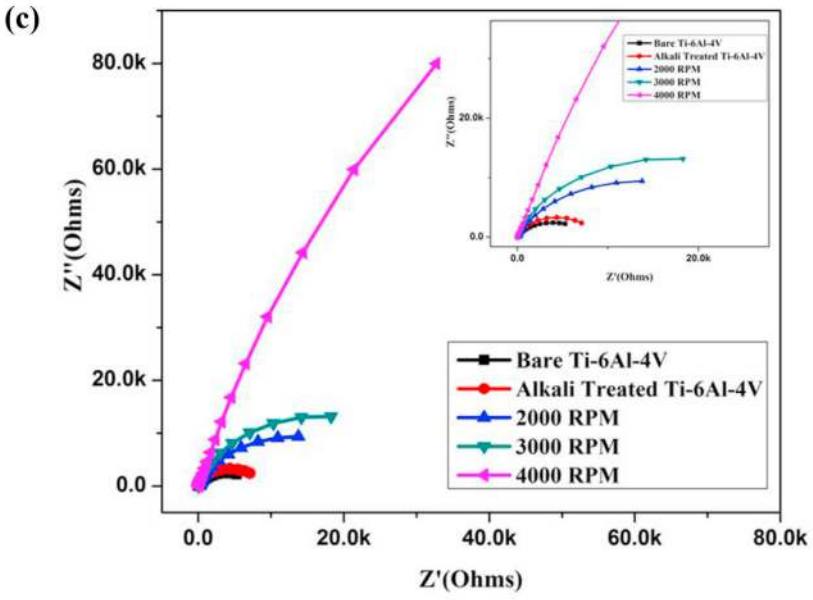
(c)
Z''(Ohms)
Z'(Ohms)
Bare Ti-6Al-4V
Alkali Treated Ti-6Al-4V
2000 RPM
3000 RPM
4000 RPM

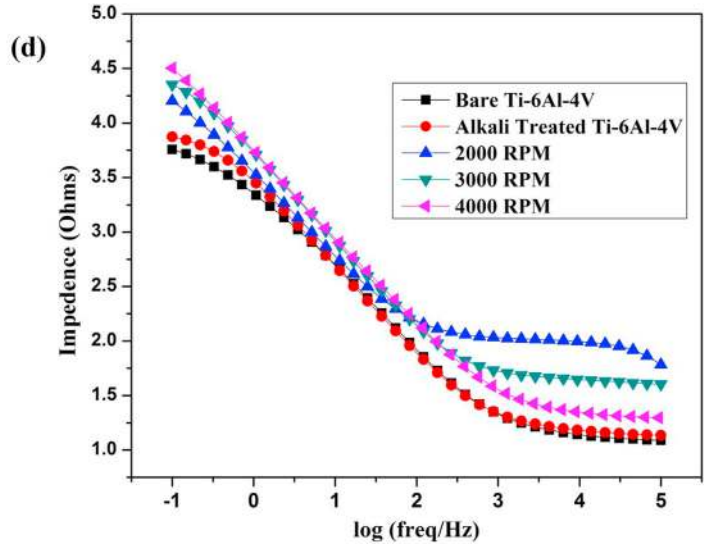
(d)
Impedence (Ohms)
log (freq/Hz)
Bare Ti-6Al-4V
Alkali Treated Ti-6Al-4V
2000 RPM
3000 RPM
4000 RPM

indentation size, the value was found to be lower with the increased load of 1.0 kgf.

This suggests that hardness measurement for different coatings exhibited different load–displacement curves, which depends on the coating characteristics such as the chemical composition of multi-layer coating thickness, porosity, voids and crack-free surface, etc. Since cracks and voids with non-uniform coating explored in 2000 RPM, it leads to less hardness than 4000 RPM. The optical microscope image for the coating produced at 4000 RPM at different indentation loads was displayed in Fig. 7. (c). Existence of crack propagation from the indented corner to the substrate surface exposed at 0.3 kgf have shown parallel and perpendicular line on the coated surface until the Ti substrates are visible. Low indentation load gives good hardness for the thin film coating for the minimum ISE.

3.8. *Potentiodynamic polarization*

Polarization studies and the electrochemical behaviour of non-coated and coated samples were identified by immersing it in SBF and evaluated using parameters like corrosion current density (I_{corr}) and corrosion potential (E_{corr}), and the values are represented in Table 2. The Tafel polarization of these samples was evaluated by cathodic and anodic slope, and the graph was displayed in Fig. 8. (b). The protection efficiency of the coating calculated by using the formula given:

$$PE = [1 - (I_{corr} / I_o)] \times 100$$

where I_{corr} is the corrosion current density of the coatings and Io is the corrosion current density of blank.

From Table 1 and Fig. 8 (b), the corrosion resistance of bare, alkali-treated Ti–6Al–4V was exhibited high corrosion current density of 0.912 μA/cm^2 and 0.832 μA/cm^2, whereas, for the coatings produced at 2000, 3000 and 4000 RPM exhibited the I_{corr} values of 0.485, 0.414 and 0.047 μA/cm^2 respectively. Compared with the bare and alkali-treated substrates, the coatings produced at different RPM showed decreased corrosion current density. These observations suggested that Ce-HAP coating showed more corrosion protection by preventing leaching out ions to the surrounding environment. Hinton et al. reported that cerium precipitate in the cathodic site by the formation of OH^- ions leading to a reduction of oxygen reaction that inhibits the corrosion. Henceforth, the cerium ions in HAP acts as a protective barrier against corrosion for long term applications.

The protection efficiency of alkali-treated Ti–6Al–4V and triple-layer coatings obtained at 2000, 3000, and 4000 RPM are 28.69%, 77.08%, 80.44% and 97.79% correspondingly. The corrosion potential (E_{corr}) of bare, alkali-treated and 2000–4000 RPM coated substrates were shown as −112.06, −97, −109, −135 and −86 mV. When compared with the bare, there was a shift in E_{corr} value, as shown in Fig. 8 (b). The E_{corr} value was towards a negative direction considerably; there was an increase in the E_{corr} value for all the coatings. Moreover, I_{corr} value was reduced extensively, and coatings act as a potential barrier to protecting the metal surface from aggressive metal ions insolation [43]. The order of corrosion restriction behaviour are as follows, 4000 RPM>3000 RPM>2000 RPM > Alkali Ti–6Al–4V > Bare-Ti-6Al–4V. Therefore, the presence of cerium ions decreases the cathodic current, and the triple-layer Ce-HAP coatings' polarization potential exhibited excellent anti-corrosion property.

3.8.1. *Electrochemical impedance spectroscopy*

The electrochemical impedance spectroscopy (EIS) is one of the prominent techniques which precisely used for understanding the protection barrier of metallic substrates. To ensure the corrosion restriction behaviour of Ce-HAP triple-layer coatings and uncoated Ti–6Al–4V alloy has been evaluated by EIS in SBF and the outcome has been discussed.

The impedance spectra from the Nyquist plots are shown in Fig. 8. (c), a well-defined capacitance loop represents interface reaction between the SBF (Electrolyte solution) and Ti–6Al–4V. It was observed that larger semicircle diameter indicated higher corrosion resistance for the coating with a higher capacitance loop than bare. The higher impedance behaviour of triple-layer coating on Ti–6Al–4V indicates consequent protection of the metal substrate from the aggressive metal ions. A higher capacitance loop corresponds to the charge transfer resistance and capacitive behaviour of coating, whereas the lower capacitive loop attribute to the corrosive products on the substrate in SBF. From the plot, it is noteworthy that all the coatings have shown significant corrosion performance in electrolyte solution than bare Ti–6Al–4V. The equivalent circuit diagram, as shown in Fig. 8 (a). The terms such as R_s, R_{ct} and C_{dl} represent the electrolyte resistance, charge transfer resistance, and double-layer capacitance. The fitting results of spectra were given in Table .3. From Table, the R_{ct} value for the bare Ti–6Al–4V was found to be 6731 Ωcm^{-1}. There was an increase in the R_{ct} value from 8871 Ωcm^{-1} to 257358 Ωcm^{-1} for the coating derived at 2000 to 4000 RPM with respect to this the C_{dl} value of the coating was found to be decreased from 85 e^{-6} to 38.77 e^{-6} F/cm^2. From the bode plot, as presented in Fig. 8. (d) Impedance spectra give an impedance of the resistor, which relies on the frequency behaviour of a capacitor. At the lower frequency region, there was a shift in the impedance resistor towards higher magnitude for triple-layer coatings. This maximum range of impedance at lower frequency is attributed to the protective metal oxide layer on the coatings preventing the metal surface from aggressive ion diffusion. An impedance behaviour of the coating obtained at 2000 RPM and 3000 RPM displayed a change in the surface state due to absorption/desorption of corrosive production on the sample or cracking of coating in the SBF solution.

The response of triple-layer Ce-HAP coating on alkali-treated Ti–6Al–4V with the non-coated sample in the SBF solution confirms the improved corrosion resistance behaviour. The inhibiting mechanism of Ce is the formation of highly insoluble cerium oxide and hydroxide is the primary inhibiting mechanism of cerium where Ce^{4+} reacts with OH^-

Fig. 8 – (a) Equivalent circuit model used for fitting (b)Tafel polarisation (c)Nyquist plot (d) and Bode plot of Bare, alkali-treated and Ce-HAP coated Ti–6Al–4V implants produced at different RPM in SBF solution.

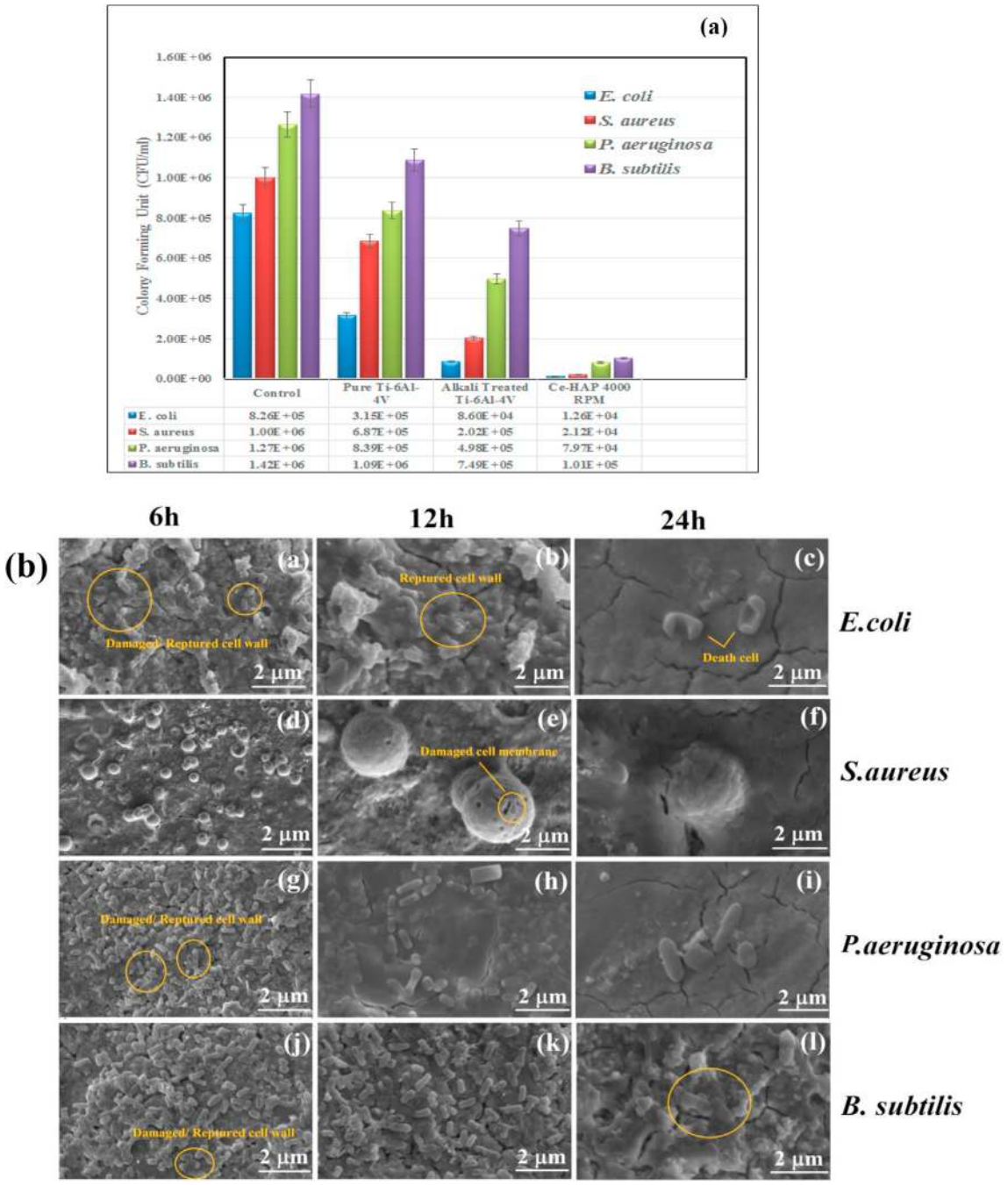

Fig. 9 – (a) The antibacterial activity of Bare Ti–6Al–4V, Alkali treated Ti–6Al–4V and Ce doped HAP coated on Ti–6Al–4V against *E. coli*, *S. aureus*, *P. aeruginosa* and *B. subtilis* pathogens. (b) The bacterial cell adhesions on Ce doped Hap coated Ti–6Al–4V produced at 4000 RPM at different incubation periods (A, B, C) 6 h (A1, B1, C1)-12 h; (A2, B2, C2)-24 h.

to form $Ce(OH)_4$. The primary inhibiting mechanism of corrosion is the reduction of H_2; there was an increase in the pH solution. When these H_2 releases, it promotes the reaction of Ce^{4+} and Ce^{3+} with OH^- and form Ce $(OH)_3$ and $Ce(OH)_4$. Superior anti-corrosion behaviour of Ce-HAP coating was as the result of the establishment of $Ce(OH)_4$ layer on the coated surface [16,44,45]. Therefore, the improvement of corrosion on Ce-HAP coated alkali-treated Ti–6Al–4V was due to the formation of insoluble cerium oxide and hydroxide in cathodic sites, thus preventing corrosion. However, in further, the complete mechanism of the cerium in corrosion has to be studied.

3.9. *Anti-bacterial activity*

The bacterial infection is the major problem associated with the implantation surgery, leading to the removal of implants caused by the contamination with sustained pain in patients and loss of functions. Anti-bacterial coatings on the implant developed to overcome implant-related problems. Thus, the

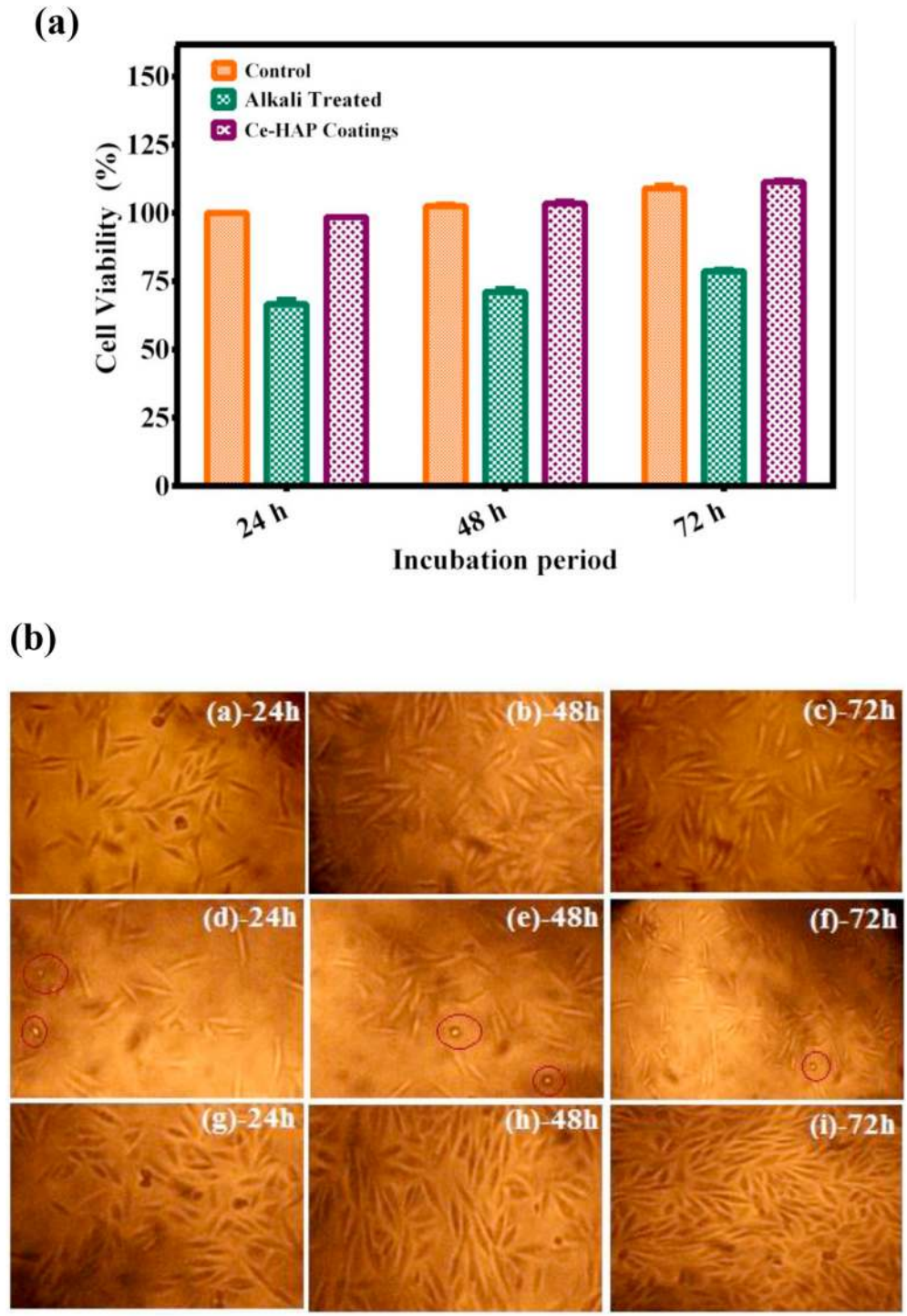

Fig. 10 – (a) The percentage of cell viability (b) The phase contrast microscopy images of MG-63 cells on alkali treated and Ce doped HAP coatings produced at 4000 RPM for 24,48 and 72 h.

study improves the surface of the implant to avoid the biofilm formation in the bacterial infection. Anti-bacterial activity of bare, alkali-treated metal and Ce-HAP coatings (4000 RPM) were evaluated for colony-forming units using gram-negative and gram-positive bacteria. Average bacterial viable counts recovered from the samples are represented in Fig. 9. (a) Control displayed cell counts of 826 $\times$ 10^3 CFU of *E.coli*, 10025 $\times$ 10^2 CFU *S. aureus* of 965 $\times$ 10^3 CFU of *P. aeruginosa* 1418 $\times$ 10^3 CFU of *B.subtilis*, after 24 h of incubations. The bare Ti–6Al–4V exhibited reduced cell counts compared to control as the result of Al and V ions that may cause toxicity to bacteria preventing bacterial growth despite significant difference over the control has experimented. The enhanced activity was renowned for the alkali-treated metal, which attributed to the formation of the TiO_2 layer on the surface, preventing bacterial development. On the other hand, great

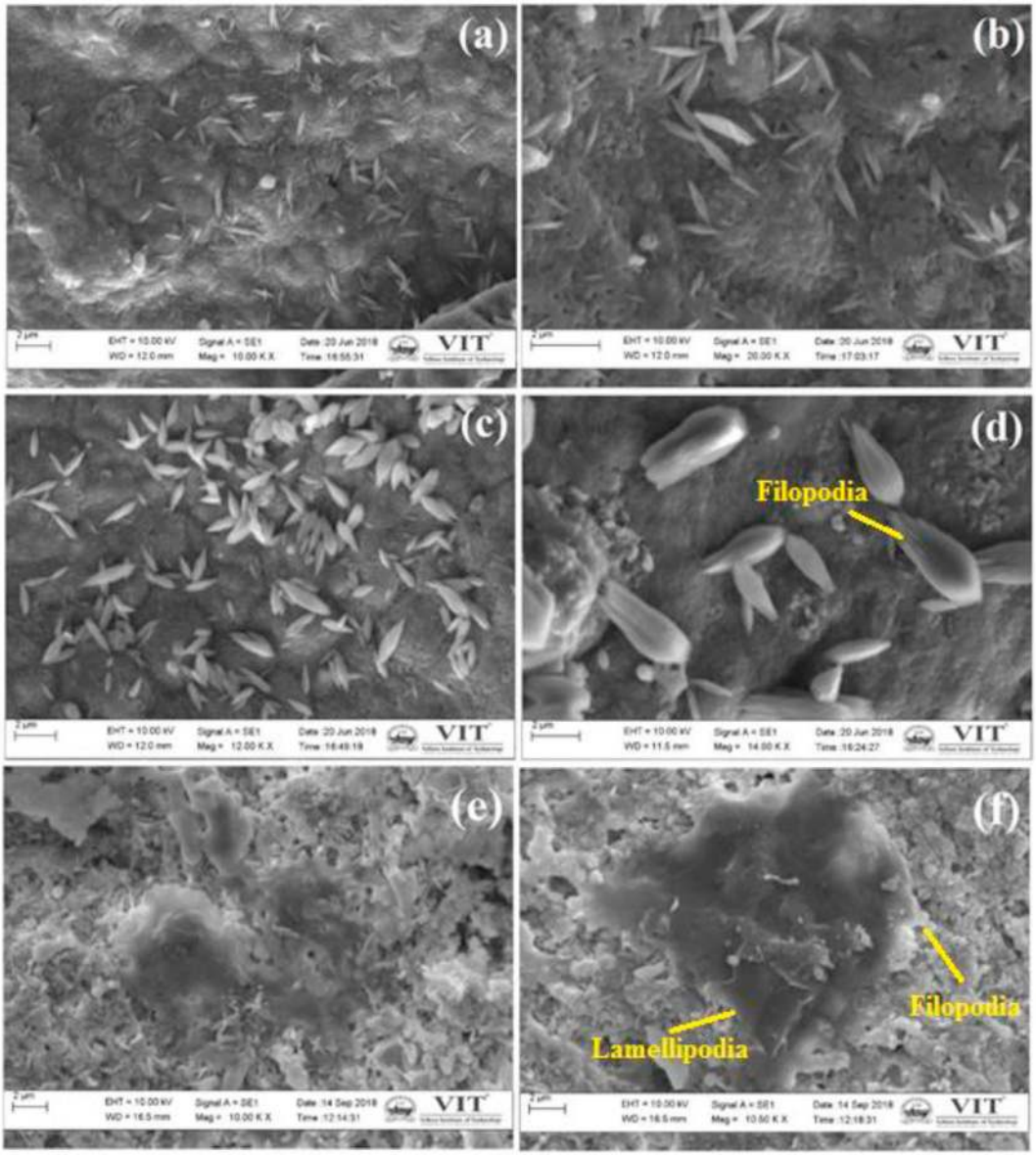

Fig. 11 – Adhesion and cell morphology of MG-63 cells on Ce doped HAP coatings produced at 4000 RPM for 24 h (a, b), 48 h (c, d) and 72 h (e, f).

exploit with a significant reduction of viable bacterial count detected for Ce-HAP coating on Ti–6Al–4V. From the previous study, it was proved that the bacterial restriction behaviour of Ce^{4+} incorporated HAP shown good pathogen inhibition activity [17]. Hence, Ce-HAP coatings on Ti–6Al–4V produced via spin coating prevented bacterial growth, making them viable for clinical applications. The order of restriction behaviour of pathogens towards coated samples as follows *E. coli* > *S. aureus* > *P. aeruginosa* > *B. subtilis*. The anti-bacterial mechanism of coatings illustrated as Ce^{4+} ions from the coatings is responsible for interfering with the membrane's permeability, respiratory chain, and enzyme inhibition. The released Ce^{4+} ions bond with the bacterial cell and cleft the cell wall through plasmolysis. These ions bind with the DNA molecules making condensation of DNA, preventing replication of DNA (specific DNA damage), protein (Polysaturated phospholipids) and enzymes. These results showed that the developed coatings considered as a promising material for orthopaedic devices.

3.10. *Bacterial adhesion*

The cell wall interaction and subsequent change in the morphology of bacteria on optimized coatings were studied for 6, 12 and 24 h, perceived using SEM analysis. Adhesion of bacterial cells on the coated metal depends on the surface properties and environmental conditions that induce the accumulation of bacteria. As shown in Fig. 9. (b), there was a significant decrease in bacterial adhesion with references to the increase in the incubation periods. The *E. coli* displayed a rod-shaped cell at 6 h of incubation, biofilm formation with bacterial cells was viewed as the time increases with a decrease in the viable cells. The bacterial cell cleavages with the leaking of cellular components are represented in Fig. 9. (b)

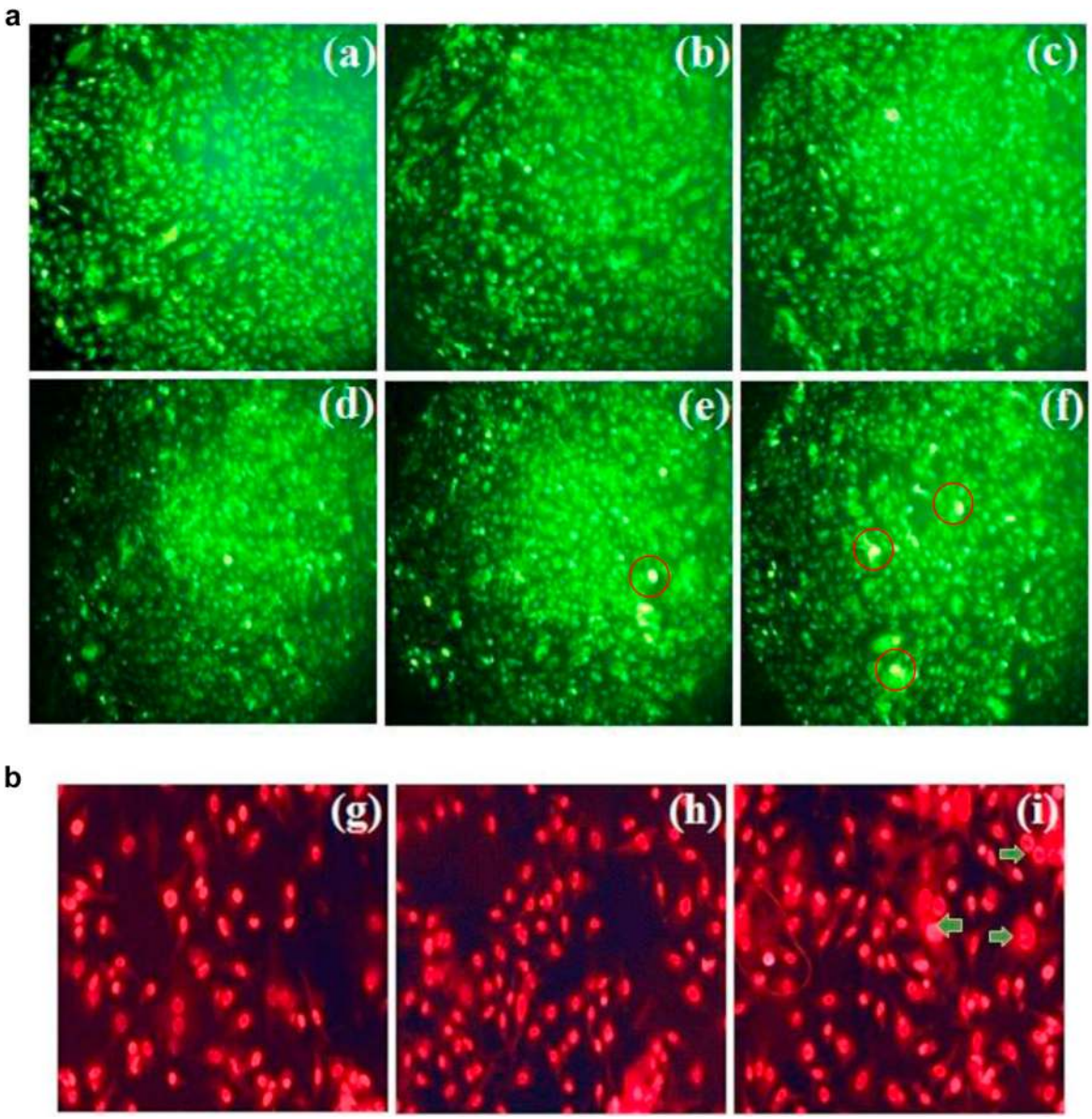

Fig. 12 – aAO/EB staining of cells treated with Ce-HAP coatings (4000 RPM) control (24 h-a; 48 h-b; 72 h-c), coatings (24 h-d; 48 h-e; 72 h -f); AO/EB staining; proapoptotic—Bright green, early apoptotic—Light green. b. Propidium iodide (PI) staining of cells treated with Ce-HAP coatings (4000 RPM) control (g), Ce-HAP coatings treated for 24 h (h) and 48 h (i). PI stained cells with abnormal nuclei, specially indicating fragmentation of nuclei/chromatin; arrow specifies apoptosis within nucleus.

S. aureus exhibited cocci shaped bacteria, shrinkage of cocci was apparent, lacking cellular content at 24 h incubation.

Damage to bacterial cell wall compromises its integrity and imbalance created on the cell wall leading to cell lysis. After incubation with Ce-HAP coating, certain bacterial cell membrane displayed burst with deep craters on their cell wall (Fig. 9b (a, b)). *S. aureus* exposed toroidal pores and hole on their cell membrane (Fig. 9b (e)). Several distinct signs of damage to the cell envelope were observed in the SEM micrographs, such as ruptured cells wall, deep craters, pores and burst cells. On the other hand, *E.coli* and *S. aureus* worked best to reveal holes and deep craters on the surface of lysed cells.

P. aeruginosa rod-shaped bacteria were responsible for infections like respiratory tract, skin and soft tissue typically in catheters. When these bacteria were treated with Ce-HAP coatings, the leached out of Ce^{4+} interact with the bacterial cell wall that induced membrane deformation, ultimately leading to bacterial death from the lag phase to the death phase. In the case of *B. subtilis*, the bacterial growth was more with rod-shaped to tapered structure along with biofilm formation was identified as shown in Fig. 9 b (i-k). However, when the incubation time periods increase, there was a drastic change in the structure of bacteria, especially protrusion of the cell wall and ruptured cell membrane. In particular,

the debris of cell death was also perceived in the electron microscope.

A more detailed morphological feature of bacteria was exposed to be of three types, from Fig. 9. (b), initially, bacterial metabolic activity increases with the biofilm formation on the implant surface with respect to the increase in the incubation period. A reduced amount of bacterial adhesion with the wrinkled cell was observed for the second type. In the third type, bacterial death occurred by ruptured cell membranes without protoplast or cellular content. However, gram-positive bacteria, the cell wall was made-up of peptidoglycan that protects the cells from rupturing, which was further modified by glycosidase and peptidase, making the cell-protective from damage. From the SEM graph, the cell morphology can be viewed while the number of cell counts was studied only by CFU, which is a quantitative assay for cell number determination. Ce-HAP coating inoculated with gram-negative and gram-positive bacteria induces cell wall distortion and plasmolysis, ultimately leading to cell death.

Therefore, in this study, the optimized Ce-HAP coating reduced bacterial adhesion, which caused the coating more bactericidal. The sequential development of antibiotic-resistant with prolonged antibiotic coatings stability in the biological environment can represent a promising material in biomedical applications.

3.11. *Cell viability assay*

It is prominent to study the biological behaviour of material to perform in the host environment. The biocompatibility of coated and non-coated implant was evaluated quantitatively by MTT assay and demonstrated in Fig. 10. (a). The study by using MG-63 osteoblast-like cell that is the most commonly used cell line because it is used to produce the interferon material with excellent growth enhancement. Figure 10. (a) displays the percentage of cell viability for alkali-treated Ti–6Al–4V metal shows 66 ± 2.20, 71 ± 1.42 and 88 ± 0.403%, which is less than the Ce-HAP coatings. The MG-63 cells showed excellent cellular activity on Ce-HAP coating (4000 RPM), as the incubation period increased from 24 h to 72 h the percentage of viability increases as 99 ± 2.12, 104 ± 2.10% and 112 ± 2.38%, respectively. The biocompatibility of alkali-treated/Ce-HAP coatings produced by the sol–gel method showed non-toxicity and enhance the proliferation of MG-63 cells. This excellent biological performance of coatings depends on the chemical composition and deposition techniques. Further, the hydroxyl group present in the HAP enhances the bioactivity by precipitation of the calcium and phosphate, thus improving the cell-to-cell interaction. Figure 10. (b) Showed that spindle-shaped cells to polygonal shape compared to the alkali-treated, Ce-HAP coating showed tremendous cell growth and the dead cell was encircled with red. Therefore, those findings proved that the Ce-HAP coatings showed prominent material for the orthopaedic applications.

3.12. *MG-63 cell adhesion*

Cell attachment plays a pivotal role in the bone-bonding ability with a coated implant for osteoblast proliferation, and differentiation and the morphology with osteoblast cell adhesion were given in Fig. 11. The result showed uniformly spread osteoblast cells on the surface of the coating with spindle-shaped morphology. From Fig. 11 (a-b), 24 h of incubation the cells appeared plate-like structure with proliferation, as the incubation period increases to 48 h (c-d) the cells showed elongated polygonal adhesion on the surface with protrusion of filopodial extensions. As elucidated in Fig (e–f) at 72 h incubation, the cells are flattened entirely on the surface along with filopodia and lamellipodia extension for cell anchoring and cell migration. The surface characteristic, for instance, wettability, roughness and surface charges play an essential role in the cell adhesion since our developed coatings were hydrophilic; it enhances the cell attachment. However, for hydrophobic surface, cells were not hindered on the surface, preventing its growth due to the airlock produced during incubation of implant that interferes with cell growth and adhesion. Cellular response on the coated metallic implants occurs in three steps: adsorption of serum protein (fibronectin cell-binding protein) on the substrates, cell–substrate interface, cell attachment and spreading by ionic/Vander walls forces. A stronger adhesion of osteoblast cells on coated metallic substrates from 24 h to 72 h of incubation was observed for the coatings. This finding shows that Ce-HAP sol–gel coatings provide an appropriate cellular attachment with the transformation of spindle-shaped morphology to the flattened structure.

3.13. *Fluorescence staining*

For long-term applications, the ceramic metal-coated implants were tested for the apoptosis of the cells by staining the cells with AO/EB and PI, as shown in Fig. 12a. and b. Apoptosis is the cell death that occurred by the characteristic change in the cells like pebbling, cell shrinkage, nuclear and chromatin fragmentation, chromatin condensation and mRNA decay and the steps of apoptosis was given in Fig. In the case of necrosis, cell death was caused by cell injury. Acridine orange is a vital dye that stains live cells as green and dead cells as orange pigments. Early apoptotic cells appear as yellow dots owing to the chromatin condensation and nuclear fragmentation [46,47]. Using Ethidium bromide stain, the cells can be differentiated from the apoptotic cell to the normal cells. The healthy cells will stain bright red nucleus, and late apoptotic cells stain orange, but, in contrast to necrotic cells, the late apoptotic cells will show condensed and often fragmented nuclei [48–50]. From Fig. 12a, the fluorescence staining showed light green staining of the nucleus without any fragmentation along with dark green cells. Ce-HAP coated on Ti–6Al–4V showed slight late apoptosis for 48 h and 72 h resulted in cellular change such as chromatic fragmentation. However, from the figure, there is no sign of necrosis (orange cells) indicating non-toxicity of the metal effects on the MG-63 osteoblast cells. This result indicates that the coated metal does not undergo any cell death. Staining the cells with PI can differentiate the normal cells from the apoptotic cells by the bright red nucleus to the fragmented DNA nucleus. As revealed in Fig. 12b. the normal cells exhibited a bright red nucleus fo r 24 h incubation without any nuclear

fragmentation as the incubation times increase to 48 h. The DNA in the nucleus shows little fragmentation resulting in DNA pattern degradation with no cell fragmentation. Conversely, no elemental response was found for necrosis resulting in the non-toxicity nature of the bioceramic metal coatings. These nuclear fragmentations from the PI staining coincide with the AO/EB staining. They showed osteoblast proliferation without any significant toxicity towards cells even after the sustained revelation of a cell on the Ce-HAP coatings.

4. Conclusions

In this present investigation, we have successfully developed sol–gel Ce-HAP coating on Ti–6Al–4V via the spin coating method.

- XRD confirms the crystallinity of the coatings with phase purity without any other secondary phases other than HAP and α-Ti without any impurity.
- Uniform, compact and crack-free coating with enhanced bioactivity was examined under the SEM micrograph for the coating derived at 4000 RPM. Contact angle measurement showed the hydrophilic nature of the coatings on the alkali-treated metal. The increased adhesion strength between coating and substrate interface was likely resulted from the formation of a chemical bond at the interface.
- CFU methods quantitatively observed the decrease in the bacterial cell growth of 1.25% Ce-HAP coatings. The order of bacterial restriction of microbes is as follows *E. coli* > *S. aureus* > *P. aeruginosa* > *B. subtilis*. Bacterial death with cell lysis and absence of cellular component was distinguished under the SEM micrograph.
- The potentiodynamic polarization and EIS studies of the substrate coated with Ce-HAP showed the superior anti-corrosive property.
- MTT assay proved excellent cell attachment and differentiation from spindle-shaped morphology to polygonal-shaped with filopodia and lamellipodia extension for anchoring cells on the coated metal substrates. AO/EB and PI staining indicate fewer effects on the cells treated with the ceramic coatings with nuclear fragmentation without any cell destruction.

Hence, the ultimate aim of the research is to produce a thin film with varying processing parameter with the improved surface property of the implant materials have been achieved for a wide range of biomedical applications.

Declaration of Competing Interest

The authors declare that they have no known competing financial interests or personal relationships that could have appeared to influence the work reported in this paper.

Acknowledgements

The authors highly acknowledge the Vellore Institute of Technology, Vellore, for rendering necessary facilities. One of the authors B. Priyadarshini thank the Council of Scientific and Industrial Research for the award of Senior Research Fellowship (09/844(0053)/2018-EMR-I) and Financial assistance. Also one of the authors Dr. U. Vijayalakshmi highly acknowledges DST, New Delhi, India (EMR/2016/002562). One of the author D. Gopi acknowledges the major financial support from the Department of Science and Technology (DST-SERB, Ref. No.:EMR/2017/003803) and University Grants Commission-Department of Atomic energy (UGC-DAE CSR, Ref. No. CSR-KN/CRS-118/2018-19/1056). S. Ramya (F.4-2/2006(BSR)/CH/17-18/0170); Dated: 25.09.2018 and E. Shinyjoy (F.4-2/2006 (BSR)/CH/18-19/0078); Dated: 06.02.2019 acknowledge the University Grants Commission for Dr. D.S. Kothari Post-Doctoral Fellowship, New Delhi, India.

Appendix A. Supplementary data

Supplementary data to this article can be found online at https://doi.org/10.1016/j.jmrt.2021.03.009.

REFERENCES

[1] Vinodhini SP, Sridhar TM. New J Chem 2019;43:7307–19.
[2] Huang CH, Huang YS, Lin YS, Lin CH, Huang JC, Chen CH, et al. Mater Sci Eng C 2014;43:343–9.
[3] Gepreel MAH, Niinomi M. J Mech Behav Biomed 2013;20:407–15.
[4] Anjaneyulu U, Priyadarshini B, Arul Xavier Stango S, Chellappa M, Geetha M, Vijayalakshmi U. Mater Technol 2017;32:800–14.
[5] Stango Arul Xavier S, Karthick D, Swaroop S, Kamachi Mudali U, Vijayalakshmi U. Ceram Int 2018;44:3149–60.
[6] Kamachimudali U, Sridhar TM. Baldev Raj, Sadhana. 2003;28:601–37.
[7] Mohammed MT, Khan ZA, Siddiquee AN. Procedia. Mater. Sci. 2014;6:1610–8.
[8] Vijayalakshmi Natarajan U, Rajeswari S. J Cryst Growth 2008;310:4601–11.
[9] Vijayalakshmi U, Rajeswari S. J Sol-Gel Sci Technol 2012;63:45–55.
[10] Zhang HB, Zhou KC, Li ZY, Huang SP. J Phys Chem Solid 2009;70:243–8.
[11] Anjaneyulu U, Deepak Pattanayak K, Vijayalakshmi U. Mater Manuf Process 2016;31:206–16.
[12] Stango Arul Xavier S, Vijayalakshmi U. Ceram Int 2019;45:69–81.
[13] Huang H, Manga Y, Huang WN, Lin CK, Tseng CL, Huang HM, et al. Mater 2018;11:1897.
[14] Eliaz N, Metoki N. Mater 2017;10:334.
[15] Yasukawa A, Gotoh K, Tanaka H, Kandori K. Colloids Surf. A Physicochem. Eng. Asp. 2012;393:53–9.

[16] Van Phuong N, Gupta M, Moon S. Prog Org Coating 2017;102:144–50.
[17] Priyadarshini B, Anjaneyulu U, Vijayalakshmi U. Mater Des 2017;119:446–55.
[18] Yingguang L, Zhuoru Y, Jiang C. J Rare Earths 2007;25:452.
[19] Yousheng O, Yushan X, Shaozao T, Qingshan S. J Rare Earths 2009;27:858.
[20] Ciobanu G, Bargan AM, Luca C. Ceram Int 2015;41:12192–201.
[21] Mathi D, Karthika R, Bharathi Priya A, Mydhili A, Gopi D, Kavitha L. Adv Nat Sci-Nanosci. 2017;11:111–6.
[22] Gopi D, Sathish kumar S, Karthika A, Kavitha L. Ind Eng Chem Res 2014;53:20145–53.
[23] Harja G Ciobanu M. Ceram Int 2019;45:2852–7.
[24] Yuan Q, Qin C, Wu J, Xu A, Zhang Z, Liao J, et al. Mater Chem Phys 2016;182:365–71. 2016.
[25] Duta L, Andrei CP. Coat 2019;9:335.
[26] Zheludkevich ML, Miranda Salvado I, Ferreira MGS. J Mater Chem 2005;15:5099–111.
[27] Harun WSW, Asri RIM, Bakar Sulong A, Che Ghani SA, Ghazalli Z. Biomedical applications and its technological facets. 2018. p. 69.
[28] Anjaneyulu U, Vijayalakshmi U. Mater Lett 2017;189:118–21.
[29] Rajeswari D, Gopi D, Ramya S, Kavitha L. RSC Adv 2014;4:61525–36.
[30] Klimova-Korsmik OG, Turichin GA, Shalnova SA, Gushchina MO, Cheverikin VV. In J. Phy.: Conference Series 2018;1109(1):012061. IOP Publishing.
[31] Lee BA, Kang CH, Vang MS, Jung YS, Piao XH, Kim OS, et al. J. Periodontal. Implant. Sci. 2012;42:248–55.
[32] El-Bagoury N, Ahmed SI, Ahmed Abu Ali O, El-Hadad S, Fallatah AM, Mersal G, et al. Materials 2019;12(8):1233.
[33] Devanand Venkatasubbu G, Ramasamy S, Ramakrishnan V. Biotechnology 2011;1:173–86.
[34] Huynh V, Ngo NK, Golden TD. Int. J. biomaterials 2019:3806504. https://doi.org/10.1155/2019/3806504.
[35] Kobayashi S, Inoue T, Nakai K. Mater Trans 2005;46:207–10.
[36] Liu X, Chu PK, Ding C. Mater. Sci. Eng: Inside R 2004;47:49–121.
[37] Hamlaoui Y, Pedraza F, Remazeilles C, Cohendoz S, Rébéré C, Tifouti L, et al. Mater Chem Phys 2009;113:650–7.
[38] Kokubo K. Acta Mater 1998;46:2519–27.
[39] Zheng S, Li J. J Sol-Gel Sci Technol 2010;54:174–87.
[40] A. Kar, K.S. Raja, M. Misra, 201(6) (2006) 3723–3731.
[41] Webb K, Hlady V, Tresco PA. J Biomed MaterRes 1998;241:422–30.
[42] Heshmatpour F, Lashteneshaee SH, Samadipour M. J Inorg Organomet Polym Mater 2018;28:2063–8. https://doi.org/10.1007/s10904-018-0864-1.
[43] Stango S, Karthick D, Swaroop S, Kamachi Mudali U, Vijayalakshmi U. Ceram Int 2018;44:3149–60.
[44] Wang R, Dangerfield R. RSC Adv 2014;4:3615–20.
[45] Saji S, Viswanathan J. Mater. Res. Technol 2019;8:5012–35.
[46] Gopalakrishnan D, Santhanam S, Baskar B, Bhuvanesh NSP, Ganeshpandian M. Appl Organomet Chem 2019;33:4756.
[47] Ananya D, Nirmala Grace A, Raghavan V. Int J Biol Macromol 2018;113:515–25.
[48] Baskar G, Lalitha K, Aiswarya R, Naveenkumar R. Mater Sci Eng, C 2018;93:809–15.
[49] Al-saran N, Subash-Babu P, Al-Nouri DM, Alfawaz HA, Alshatwi AA. Environ Toxicol Pharmacol 2016;47:19–27.
[50] Srivastava S, Kumar N, Thakur RS, Roy P. Biol Trace Elem Res 2013;152:135–42.